



# An energetically consistent tension–compression split for phase-field models of fracture at large deformations

Shreeraman Swamynathan<sup>a,b,\*</sup>, Sebastian Jobst<sup>b</sup>, Marc-André Keip<sup>a</sup>

<sup>a</sup> Institute of Applied Mechanics, University of Stuttgart, Pfaffenwaldring 7, 70569 Stuttgart, Germany

<sup>b</sup> Robert Bosch GmbH, Markwiesenstraße 46, 72770 Reutlingen, Germany

## ARTICLE INFO

### Keywords:

Phase-field modeling of fracture  
Tension–compression split  
Energy-consistency  
Finite deformations  
Soft materials

## ABSTRACT

The predictive description of fracture has been an important topic of research over the last decades. In this context, the recently developed phase-field approach to fracture has proven to be an efficient and versatile tool in handling arbitrary and topologically complex crack patterns in an adequate manner. However, open problems reside in the distinction between tensile and compressive states in the framework of energetically driven crack evolution, especially at finite deformations. In the present contribution, a novel methodology to split energy-density functions is proposed that can be applied to a large variety of polyconvex energies. The applicability of the proposed formulation is validated by a series of numerical examples involving small and large deformations, in which we also provide comparisons with existing splits from literature.

## 1. Introduction

Elastomers and rubber-like materials find usage in a wide range of industrial sectors such as automotive, aerospace, biomedical, construction and soft robotics. Owing to their ability to undergo large elastic deformations under relatively small stresses, they are particularly suitable in designing parts that experience cyclic loadings; for example, adhesive sealants, shock absorbers, tyres and engine mounts. The choice of the material depends largely on application-specific requirements in terms of the reliability and lifetime of the components under real-life loading conditions. Therein, the need for understanding the material behavior and the ability to predict the failure due to crack initiation and propagation in elastomeric materials is of paramount importance.

The classical theory of fracture mechanics traces back to Griffith (1921) and provides criteria for propagation of an existing crack subjected to prescribed loading conditions. Nevertheless, they are not self-contained in the sense that additional criteria are required to determine in which direction a crack will propagate and by how much. Moreover, they are known to fail in the prediction of crack initiation.

The recently developed *phase-field approach to fracture* emerging from the seminal work of Francfort and Marigo (1998) has been known to overcome the above drawbacks as it is completely based on energy minimization in a variational setting. The numerical implementation of the variational approach to brittle fracture was described in Bourdin et al. (2000), where a small positive length scale parameter ( $l$ ) characterizing the width of a diffuse crack zone was introduced. This

approximation regularizes a sharp crack surface by a diffuse crack, wherein in the limit  $l \rightarrow 0$  the sharp crack topology is retrieved.

In the recent past, several extensions of the phase-field approach to fracture have been developed. The extension from brittle to ductile fracture has been treated among others by Kuhn et al. (2016) at small deformations and by Miehe et al. (2015a) and Ambati et al. (2016) at finite deformations. An extension towards brittle fracture in anisotropic solids has been discussed in Teichtmeister et al. (2017) and Bleyer and Alessi (2018). Developments of phase-field models to simulate dynamic fracture have been reported among others in Gürses and Miehe (2009), Bourdin et al. (2011) and Hofacker and Miehe (2012). Extensions to finite deformations have been reported in Hesch and Weinberg (2014), Miehe and Schänzel (2014), Gültekin et al. (2016) and Raina and Miehe (2016) to name only a few.

In all cases it is important to distinguish between tensile and compressive states of the material in order to ensure that cracks propagate only under tensile loadings. We highlight the ideas of Amor et al. (2009) and Miehe et al. (2010a) in the framework of small deformations. Recently, the shortcomings of these approaches were shown in Strobl and Seelig (2015) and solutions based on accounting for crack direction and directional decomposition of stresses were suggested in Strobl and Seelig (2016), Steinke and Kaliske (2019) and Storm et al. (2020) respectively. Associated approaches in the finite-strain regime

\* Corresponding author at: Institute of Applied Mechanics, University of Stuttgart, Pfaffenwaldring 7, 70569 Stuttgart, Germany.

E-mail address: [shreeraman.swamynathan@mechbau.uni-stuttgart.de](mailto:shreeraman.swamynathan@mechbau.uni-stuttgart.de) (S. Swamynathan).

were provided, for example, by Hesch and Weinberg (2014), Hesch et al. (2017), Bilgen and Weinberg (2019), Tang et al. (2019) and Yin and Kaliske (2020).

The large variety of approaches documented above indicates that tension–compression splits are by no means unique. In fact, each approach comes with its own advantages but also with its own limitations. The situation seems particularly delicate at large deformations, where the definition of tensile and compressive energy states is less intuitive. In that respect, the purpose of the present contribution is two-fold. Firstly, it is our goal to propose a novel decomposition of an energy density into tensile and compressive parts, wherein the energy required to create new crack surfaces is entirely compensated from the tensile part of the underlying energy-density function. Secondly, we aim at a versatile framework that allows the application to a large variety of hyperelastic models<sup>1</sup> based on the whole set of irreducible invariants of some deformation tensor.

The paper is structured as follows. In Section 2, we briefly recall the phase-field formulation of brittle fracturing in a variational setting in the sense of Miehe et al. (2010a,b). We begin by defining the primary fields of the multi-field problem. Thereafter, we provide the constitutive ingredients of the formulation and comment on the need to appropriately split the free-energy function into tensile and compressive parts. Finally, coupled evolution equations of the multi-field problem are derived and the numerical implementation is shortly discussed. In Section 3, a brief overview of existing splits in the context of energy-driven cracks is presented. Here, we restrict ourselves specifically to formulations applicable in the finite-deformation regime. Coupled forms of energy-density functions are described for each case, with appropriate definitions of the variational crack-driving energy. A qualitative and quantitative comparison of the explicated models by simulating relevant numerical examples is done in Section 4. Simulations in conjunction with a polyconvex Mooney–Rivlin model demonstrate the applicability to physically realistic nonlinear models in consideration of large strains. Section 5 summarizes the main ideas of the present contribution and provides pointers for future work.

## 2. Governing equations of the phase-field approach to fracture

In the present section, we describe the phase-field formulation of fracture for large-deformation kinematics. We provide an overview of the governing equations for the case of energetically driven fracture evolution. In what follows, we adopt the geometric description of diffuse fracture motivated by Miehe et al. (2010a,b).

### 2.1. Framework and kinematics of the multi-field problem

We begin by providing a framework that allows for the treatment of fracture evolution in soft materials. Let  $B \subset \mathcal{R}^\theta$  be a solid body (with  $\theta$  being the spatial dimension) in its reference configuration with spatial coordinates  $X \in B$  at time  $t \in \mathcal{T}$ . To this end, we consider as independent fields a sufficiently smooth deformation map and a damage phase-field given by

$$\varphi : \begin{cases} B \times \mathcal{T} & \rightarrow \mathcal{R}^\theta \\ (X, t) & \mapsto \varphi(X, t) \end{cases} \quad \text{and} \quad d : \begin{cases} B \times \mathcal{T} & \rightarrow \mathcal{R} \in [0, 1] \\ (X, t) & \mapsto d(X, t), \end{cases} \quad (1)$$

where ‘ $\varphi$ ’ maps material points  $X \in B$  at time  $t \in \mathcal{T}$  to points  $x = \varphi(X, t)$  and ‘ $d$ ’ accounts for an evolving crack set  $\Gamma \subset \mathcal{R}^{\theta-1}$ . Based on the mapping we define the deformation gradient and its determinant

respectively as

$$F := \frac{\partial \varphi}{\partial X} = \nabla \varphi \quad \text{and} \quad J = \det(F) > 0. \quad (2)$$

The phase-field  $d$  takes values of  $d(X, t) = 0$  denoting the unbroken and  $d(X, t) = 1$  denoting the completely broken state of the material for every point  $X \in B$  at time  $t \in \mathcal{T}$ . It is with this fracture phase-field, a sharp crack  $\Gamma$  is regularized by its diffuse counterpart  $\Gamma_l$  using the internal length-scale parameter  $l$ . Please see Fig. 1 for an illustration.

Now, in accordance with Miehe et al. (2010a,b), we postulate the existence of a rate-type<sup>2</sup> potential  $\Pi$  formally given as

$$\Pi(\dot{\varphi}, \dot{d}; \varphi, d) = \Pi_{\text{int}}(\dot{\varphi}, \dot{d}; \varphi, d) - \mathcal{L}(\dot{\varphi}), \quad (3)$$

wherein  $\Pi_{\text{int}}$  denotes an internal-power functional, that is balanced by the external-power functional  $\mathcal{L}$  formulated as

$$\mathcal{L}(\dot{\varphi}) = \int_B \bar{\gamma} \cdot \dot{\varphi} \, dV + \int_{\partial B_l} \bar{\tau} \cdot \dot{\varphi} \, dA, \quad (4)$$

where  $\bar{\gamma}$  and  $\bar{\tau}$  are prescribed body forces and surface tractions respectively. The internal-power functional is defined as below

$$\Pi_{\text{int}}(\dot{\varphi}, \dot{d}; \varphi, d) = \frac{d}{dt} [E(\varphi, d)] + D(\dot{d}), \quad (5)$$

in terms of the time rate of the internal-energy functional  $E(\varphi, d)$  and dissipation functional  $D(\dot{d})$ . The dissipation functional is defined in terms of a dissipation-density function  $\Phi(\dot{d})$  as

$$D(\dot{d}) = \int_B \Phi(\dot{d}) \, dV, \quad (6)$$

where the dissipation due to diffuse crack-topology is inherently accounted for. In order to guarantee irreversibility of fracture evolution, we adopt the non-smooth dissipation-density function (Miehe et al., 2010a,b)

$$\Phi(\dot{d}) = \frac{d}{dt} [W_c(d)] + I(\dot{d}) + \frac{\eta}{2} \dot{d}^2 \quad (7)$$

in terms of the non-smooth indicator function

$$I(\dot{d}) = \begin{cases} 0 & \text{for } \dot{d} \geq 0 \\ \infty & \text{otherwise} \end{cases} \quad \text{with} \quad \partial_d I(\dot{d}) = \begin{cases} 0 & \text{for } \dot{d} > 0 \\ \mathcal{R}_- & \text{for } \dot{d} = 0 \end{cases} \quad (8)$$

and a viscous term with viscosity parameter  $\eta$  with units  $\text{Ns/mm}^2$ . The regularized crack work functional  $W_c(d)$  is motivated from Griffith’s theory, which dictates that the energy required to create a sharp crack surface  $\Gamma$  is given by  $\int_\Gamma g_c \, d\Gamma$ , where  $g_c$  is the critical energy-release rate (Griffith, 1921). Analogously, the work required to create a regularized crack surface  $\Gamma_l(d)$  can be given by

$$W_c(d) = \int_B g_c \gamma_l(d, \nabla d) \, dV, \quad (9)$$

where  $\gamma_l(d, \nabla d)$  is the crack-surface-density function as defined in Miehe et al. (2010a).

The energy-storage functional  $E(\varphi, d)$  in the internal-power functional (see Eq. (5)) is defined in terms of a volume-specific energy-density function  $\hat{\psi}(F, d)$  as

$$E(\varphi, d) = \int_B \hat{\psi}(F, d) \, dV, \quad (10)$$

where  $\hat{\psi}(F, d)$  can be computed from an initially undamaged energy-density function  $\hat{\psi}_0(F)$  by means of a degradation function  $g(d)$  as<sup>3</sup>

$$\hat{\psi}(F, d) := [g(d) + k] \hat{\psi}_0(F). \quad (11)$$

<sup>1</sup> We concentrate on the models where the strain-energy function is given in terms of the invariants. The validity of this approach to models expressed as functions of principal stretches are not investigated here.

<sup>2</sup> Time rates are denoted by  $\dot{\diamond} := \frac{d}{dt} \diamond$ .

<sup>3</sup> The parameter  $k \approx 0$  is a small positive number that prevents ill-posedness at  $d = 1$ .

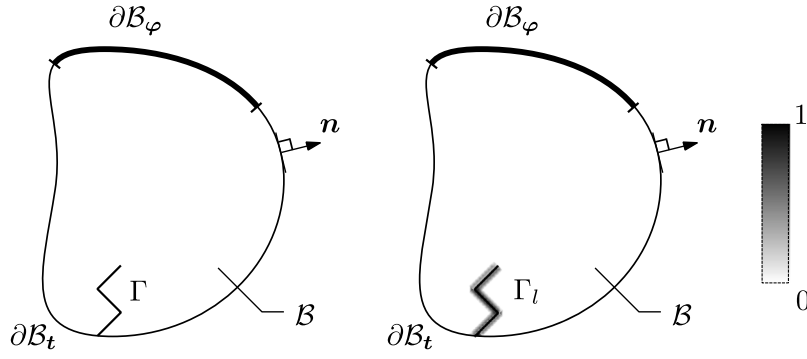


Fig. 1. Schematic of a fractured body  $B$  containing a sharp and a diffuse crack. (a) The body containing a sharp crack  $\Gamma$  modeled as internal discontinuity and (b) the same body containing a diffuse crack  $\Gamma_l$  approximated by the crack phase-field ( $d$ ).

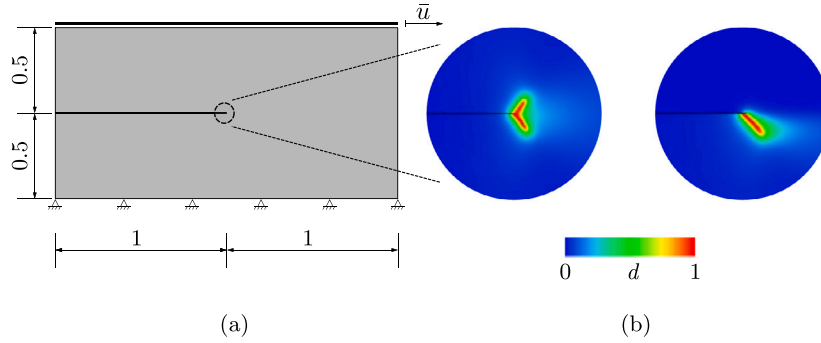


Fig. 2. Fracture evolution with and without tension-compression split. (a) Boundary-value problem representing a simple-shear test on a pre-notched specimen as considered in Mische et al. (2010b) (units in mm). (b) Contour plots of damage phase field obtained for degradation of the total energy function as in (11) (left circle) and for degradation of only the tensile part of the energy as in (13) (right circle).

The degradation function  $g(d)$  is a monotonically decreasing function with the properties  $g(0) = 1$ ,  $g(1) = 0$  and  $\frac{d}{dd}g(d)|_{d=1} = 0$ , see Kuhn et al. (2015). In what follows we adopt the quadratic form

$$g(d) = (1 - d)^2. \quad (12)$$

As a result of definition (11) the above formulation would result in fracturing also under a compressive state of the material and thus lead to unphysical crack patterns. In order to constrain fracture propagation to tensile states of the material, one usually splits the undamaged energy-density function  $\hat{\psi}_0(F)$  into a tensile and a compressive part  $\hat{\psi}_0^+(F)$  and  $\hat{\psi}_0^-(F)$  respectively. By doing so, the energy required to create new crack surfaces is compensated by the tensile energy only. Formally, we arrive at such a setting by defining the energy-density function as

$$\psi^e(F, d) = g(d)\psi_0^+(F) + \psi_0^-(F). \quad (13)$$

To demonstrate the above mentioned phenomena, we consider the pure-shear test documented in Mische et al. (2010b) and plot corresponding results in Fig. 2. We observe that by degrading the complete energy density according to Eq. (11), we obtain an unphysical symmetric crack branching. When the degradation is applied to the tensile part only according to Eq. (13), a physically reasonable crack pattern is obtained.

With all the ingredients at hand, minimizing the total potential functional (3) with respect to the unknown field variables yields the complete set of coupled governing equations in the domain  $B$  with associated boundary conditions. Upon mathematical simplifications the governing equations reduce to a compact system of two equations given by

$$\text{Div}[\mathbf{P}(F, d)] + \tilde{\gamma} = \mathbf{0} \quad \text{and} \quad g_c \delta_d \gamma_l(d) + \eta d - 2(1 - d)H = 0, \quad (14)$$

where  $\mathbf{P}(F, d) = \partial_F \psi(F, d)$  is the Piola stress tensor,  $\delta_d \gamma_l(d) = \partial_d \gamma_l - \text{Div} \partial_{\nabla d} \gamma_l$  is the variational derivative of the crack-surface-density function with respect to the phase field. In Eq. (14), crack growth is clearly governed by the last term wherein we introduce formally a local history-field  $H$ . The parameter  $H$  is defined as  $H(X, t) = \max_{\tau \in [0, t]} \psi_0^+[F(X, \tau)]$  which denotes the maximum positive undamaged energy density reached during the entire loading history of the material in time  $[0, t]$ . For detailed motivation of such an approach, we refer to the work of Mische et al. (2010a).

### 3. Energetically consistent tension-compression split of the free energy

We now substantiate the above discussed tension-compression split of the energy density (13) by proposing a new *energetically consistent split* that allows for the consideration of a *variety of hyperelastic material models at large deformations*. In order to highlight the salient features of the proposed methodology, we compare it with established variants from literature. To be specific, we take into account the models suggested by Hesch et al. (2017), Tang et al. (2019) and a model that is inspired by the work of Amor et al. (2009). We do not consider the multiplicative split proposed in Hesch and Weinberg (2014), as in such an approach, the rank-one convexity of the strain-energy functional is not always guaranteed. This has been shown to be numerically not very robust by Hesch et al. (2017, see Remark 4). To put the comparison into perspective, we first provide brief descriptions of the associated models in the following.

#### 3.1. The large-strain model of Tang et al. (2019) (Model 1)

In a recent paper, Tang et al. (2019) presented a novel way to decompose the strain energy in the context of the large-strain phase-field

modeling of fracturing. To take into account the different contributions of tension and compression, the authors proposed the additive decomposition of a neo-Hookean strain-energy density according to

$$\hat{\psi}(I_1, J) = \hat{\psi}_1(\lambda_i) + \hat{\psi}_2(J), \quad (15)$$

where  $I_1 = \text{tr}(\mathbf{F}^T \mathbf{F})$ ,  $J = \det \mathbf{F}$  and  $\lambda_i$  corresponds to the  $i^{\text{th}}$  principal stretch. The first term of (15) accommodates contributions from each of the individual principal stretches and the second term takes account of the volumetric deformation. Tang et al. (2019) selected a particular form of the neo-Hookean energy-density function given by

$$\psi_{\text{NH}} = \frac{\mu}{2}(I_1 - 3 - 2 \ln J) + \frac{\kappa}{2}(\ln J)^2. \quad (16)$$

This function can be recast into the form

$$\psi_0 = \frac{\mu}{2} \sum_{i=1}^3 (\lambda_i^2 - 1 - 2 \ln \lambda_i) + \frac{\kappa}{2}(\ln J)^2, \quad (17)$$

where the individual contributions can be identified with those given in Eq. (15). To ensure a consistent tension–compression split, the above energy density is divided into tensile and compressive contributions according to

$$\psi_0(\mathbf{F}) = \psi_0^+(\mathbf{F}) + \psi_0^-(\mathbf{F}), \quad (18)$$

where  $\psi_0^+(\mathbf{F})$  and  $\psi_0^-(\mathbf{F})$  are defined as

$$\psi_0^+(\mathbf{F}) = \psi_0(\lambda_i^+, J^+) \quad \text{and} \quad \psi_0^-(\mathbf{F}) = \psi_0(\lambda_i^-, J^-)$$

where for  $\diamond := \{\lambda_i, J\}$

$$\diamond^+ = \begin{cases} \diamond & \text{when } \diamond \geq 1 \\ 1 & \text{when } \diamond < 1 \end{cases} \quad \text{and} \quad \diamond^- = \begin{cases} \diamond & \text{when } \diamond < 1 \\ 1 & \text{when } \diamond \geq 1 \end{cases} \quad (19)$$

With the proposed split at hand, the local state of a material point is considered to be either under tension or compression. The final definition of the energy-density function is then given in the classical format by

$$\psi(\mathbf{F}, d) = g(d)\psi_0^+(\mathbf{F}) + \psi_0^-(\mathbf{F}), \quad (20)$$

where the degradation function  $g(d)$  defined in Eq. (12) acts only on the tensile part of the energy density.

The split proposed by Tang et al. (2019) could be validated by the authors by means of a series of boundary value problems involving complex fracture patterns. We however note that the split is based on the requirement that the underlying energy density needs to be recast into the generic form given in Eq. (15). This may not be straightforward (if not impossible) for arbitrary energy densities and thus limits the applicability of the proposed approach.

### 3.2. Large-strain model inspired from Amor et al. (2009) (Model 2)

As a further reference model for comparison we adopt the ideas of Amor et al. (2009) and transfer them to the consideration of large strains.<sup>4</sup> In order to do so we employ the following split of the energy-density function into an isochoric and a volumetric part

$$\psi_0(\mathbf{F}, J) = \psi_{\text{iso}}(\bar{\mathbf{I}}_1) + \psi_{\text{vol}}(J), \quad (21)$$

where  $\bar{\mathbf{I}}_1 = \text{tr}(\bar{\mathbf{C}})$  is the first invariant of the unimodular part of the right Cauchy–Green deformation tensor

$$\bar{\mathbf{C}} = \bar{\mathbf{F}}^T \bar{\mathbf{F}} = J^{-2/3} \mathbf{F}^T \mathbf{F}.$$

We assume that the isochoric part of the energy-density function (21) always contributes to the creation of new fracture surfaces. In order to distinguish between tension and compression, we proceed similar to

Amor et al. (2009) and consider the magnitude of the volumetric strain for that distinction.<sup>5</sup> Accordingly, we split the volumetric part of the energy-density function into

$$\psi_{\text{vol}}(J) = \psi_{\text{vol}}^+(J^+) + \psi_{\text{vol}}^-(J^-) \quad (22)$$

where the individual energy contributions are formulated in terms of the Heaviside function  $H$  as

$$\psi_{\text{vol}}^+ = H(J - 1)\psi_{\text{vol}} \quad \text{and} \quad \psi_{\text{vol}}^- = [1 - H(J - 1)]\psi_{\text{vol}}.$$

The final form of the coupled free energy function is then given by

$$\psi(\mathbf{F}, d) = g(d)[\psi_{\text{iso}}(\bar{\mathbf{I}}_1) + \psi_{\text{vol}}^+(J^+) + \psi_{\text{vol}}^-(J^-). \quad (23)$$

It is clear from the above model that isochoric deformations always provide a source for the creation of cracks. However, although only the tensile volumetric deformations are taken into account in the degradation, the resulting model does not completely prohibit local damage evolution under compression as will be shown in a numerical example in Section 4.2. In what follows, we propose an energetically consistent split that eliminates this behavior and is also transferable to complex hyperelastic energy functions.

### 3.3. Energetically consistent large-strain model (Model 3)

To come up with a model that preserves the compressive stiffness of the material and that allows for the evolution of the phase field under a local state of tension, we follow the invariant-based approach of Hesch et al. (2017) and decompose the energy function into isochoric and volumetric parts as follows

$$\psi_0(\bar{\mathbf{I}}_1, \bar{\mathbf{I}}_2, J) = \psi_{\text{iso}}(\bar{\mathbf{I}}_1, \bar{\mathbf{I}}_2) + \psi_{\text{vol}}(J).$$

Here,  $\bar{\mathbf{I}}_1$  and  $\bar{\mathbf{I}}_2$  are the first and the second invariant of the isochoric part of the right Cauchy–Green deformation tensor given by

$$\bar{\mathbf{I}}_1 = \text{tr} \bar{\mathbf{C}} = J^{-2/3} I_1 \quad \text{and} \quad \bar{\mathbf{I}}_2 = \text{tr}(\text{cof } \bar{\mathbf{C}}) = J^{-4/3} I_2,$$

where  $I_1$  and  $I_2$  are the first and second invariant of the right Cauchy–Green tensor and  $\text{cof}(\bullet)$  denotes the cofactor of  $(\bullet)$ . As usual, we split the undamaged energy density into tensile and compressive contributions

$$\psi(\bar{\mathbf{I}}_1, \bar{\mathbf{I}}_2, J) = \psi_{\text{iso}}^+(\bar{\mathbf{I}}_1^+, \bar{\mathbf{I}}_2^+) + \psi_{\text{vol}}^+(J^+) + \psi_{\text{iso}}^-(\bar{\mathbf{I}}_1^-, \bar{\mathbf{I}}_2^-) + \psi_{\text{vol}}^-(J^-) \quad (24)$$

wherein positive and negative parts of energies are defined using the Heaviside functions as

$$\begin{aligned} \psi_{\text{iso}}^+ &= \sum_i H(I_i - 3) \psi_{\text{iso}}(\bar{\mathbf{I}}_i) \\ \psi_{\text{iso}}^- &= \sum_i [1 - H(I_i - 3)] \psi_{\text{iso}}(\bar{\mathbf{I}}_i), \end{aligned} \quad (25)$$

with ‘ $i$ ’  $\in [1, 2]$  denoting the corresponding invariant. In cases involving the product of two invariants, we explicitly state that the product term contributes to the positive energy only when the associated condition in (25) is satisfied by both the invariants. Furthermore, the Jacobian is split in the sense of Tang et al. (2019) via the decomposition (19). Using the proposed splits, the final form of the energy function reads as<sup>6</sup>

$$\psi(\mathbf{F}, d) = g(d)[\psi_{\text{iso}}^+(\bar{\mathbf{I}}_1^+, \bar{\mathbf{I}}_2^+) + \psi_{\text{vol}}^+(J^+) + \psi_{\text{iso}}^-(\bar{\mathbf{I}}_1^-, \bar{\mathbf{I}}_2^-) + \psi_{\text{vol}}^-(J^-)] \quad (26)$$

Additionally, the first Piola stress tensor is decomposed independent of the energy function as

$$\mathbf{P}^+ = \sum_i H(\bar{\mathbf{I}}_i - 3) \mathbf{P} \quad \text{and} \quad \mathbf{P}^- = \sum_i [1 - H(\bar{\mathbf{I}}_i - 3)] \mathbf{P} \quad (27)$$

based on the isochoric invariants of the deformation tensor.

<sup>4</sup> The original model of Amor et al. (2009) was developed in the context of linear elasticity. We perform a simple extension towards finite elasticity, see Tang et al. (2019) for a similar treatment.

<sup>5</sup> In their original paper, Amor et al. (2009) distinguish tension and compression by means of the trace of the linear strain tensor.

<sup>6</sup> We note that by using the above split, we preserve the polyconvexity of the energy function in the sense of Ball (1976), see also Hesch et al. (2017).

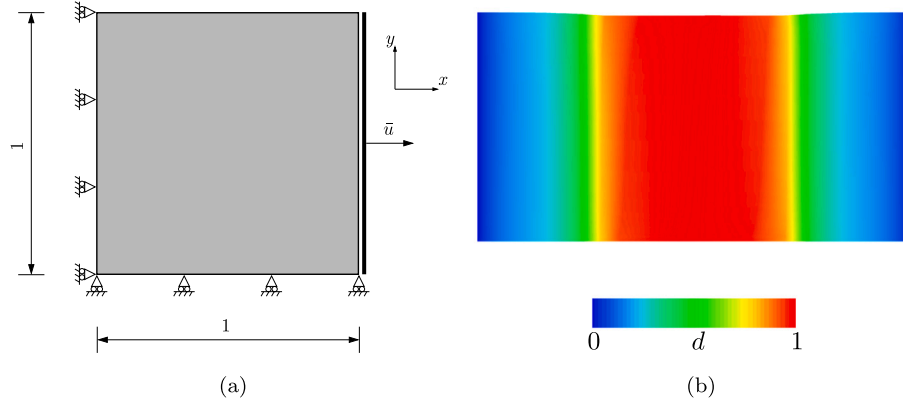


Fig. 3. Tension test employed for the validation of our numerical implementation of the model of Tang et al. (2019). (a) Geometry and boundary conditions of the specimen as in Tang et al. (2019) and (b) evolved damage phase field at imposed displacement of  $\bar{u} = 0.801$  mm.

**Remark 1.** As mentioned earlier, the above proposed split is based on the work of Hesch et al. (2017), who were the first to come up with the idea of splitting the invariants of the deformation tensor rather than working with individual stretches. The crucial difference between their model and the model proposed above lies in the fact that, using the above split, the sum of the individual tensile and compressive energy terms consistently add up to the total energy function. That means that with the above proposed model we always satisfy the conditions

$$\begin{aligned}\psi_{\text{iso}}(\bar{I}_1, \bar{I}_2) &= \psi_{\text{iso}}^+(\bar{I}_1^+, \bar{I}_2^+) + \psi_{\text{iso}}^-(\bar{I}_1^-, \bar{I}_2^-), \\ \psi_{\text{vol}}(J) &= \psi_{\text{vol}}^+(J^+) + \psi_{\text{vol}}^-(J^-).\end{aligned}\quad (28)$$

This consistency is not strictly fulfilled when using the approach of Hesch et al. (2017), see also the discussion in Bilgen and Weinberg (2019, Section 3). To elucidate the difference, let us consider the simple case of a compressible neo-Hookean model that is split into isochoric and volumetric parts as

$$\psi_{\text{NH}}(\bar{I}_1, J) = \frac{\mu}{2}(\bar{I}_1 - 3) + \frac{\kappa}{2}(J - 1)^2. \quad (29)$$

Let us further assume that  $I_1 > 3$  and  $J < 1$ . Then, based on the above proposed split, we have

$$\begin{aligned}\psi_{\text{iso}}^+(\bar{I}_1^+) &= \frac{\mu}{2}(\bar{I}_1 - 3), \quad \psi_{\text{iso}}^-(\bar{I}_1^-) = 0, \quad \psi_{\text{vol}}^+(J^+) = 0, \\ \psi_{\text{vol}}^-(J^-) &= \frac{\kappa}{2}(J - 1)^2,\end{aligned}$$

so that condition (28) is satisfied. The same can be verified for other combinations of  $I_1$  and  $J$ . In contrast, when one employs the method proposed in Hesch et al. (2017, Refer Eq. 54, therein) and repeats the above calculation, it can be seen that condition (28) is not satisfied.

**Remark 2.** On first sight, the above enhancement of the invariant-based split of Hesch et al. (2017) seems only minor and of little importance. We however note that an energetically consistent split, in which tensile and compressive parts consistently add up to the total energy, is of major relevance for a number of implementations of variationally consistent material models. By formulating the energy functional consistently, the resulting governing equations maintain a physically meaningful structure.

#### 4. Results and discussion

The present section is devoted to analyzing the modeling capabilities of each of the splits explained in Section 3. We provide both qualitative and quantitative comparisons by presenting representative numerical examples in consideration of small and finite deformations. Here, we restrict ourselves to investigating boundary value problems, where the effect of the individual split is readily distinguishable. The performance of the proposed energetically consistent model (Section 3.3)

is validated by comparing with the remaining models (discussed in Sections 3.1 and 3.2) and the advantages of the newly proposed split are emphasized.

The simulations documented below are based on numerical implementations into the finite-element program FEAP (Taylor, 2017). Concerning time discretization, we adopted the one-pass operator splitting algorithm according to Miehe et al. (2010a). This algorithm permits an alternating staggered update of the fracture phase field and the deformation field. For more details on the algorithmic formulation we refer to Miehe et al. (2010a).

We start by validating our numerical implementation of the model of Tang et al. (2019) (Section 4.1). Subsequently we compare the three models by considering a classical single-edge-notched shear test (Section 4.2) and a three-point bending test (Section 4.3). While the study of the former problems will entirely be based on neo-Hookean energy densities, we will also present numerical examples in consideration of a Mooney–Rivlin-type energy. Here, we again study the three-point bending test (Section 4.4) and then analyze a complex boundary value problem in terms of an inhomogeneous strip under tension (Section 4.5). Throughout the following two-dimensional examples, plane-strain conditions are assumed.

##### 4.1. Validation of the numerical implementation of the model of Tang et al. (2019)

Before we begin with the comparison of results obtained from the different splits, the numerical implementation of the model of Tang et al. (2019) discussed in Section 3.1 is first validated here. To this end, we simulate the example of uniaxial tension as in Section 3.1 of their work. To be specific, we consider a square block (please refer to Fig. 3a), whose left edge is constrained in horizontal  $x$ -direction and whose bottom edge is constrained in vertical  $y$ -direction. The right edge is loaded along the  $x$ -direction with homogeneous Dirichlet condition for the phase field (i.e.,  $d = 0$ ) being imposed on the left and the right edge. The material parameters used for the simulation are  $E = 14.5$  MPa,  $\nu = 0.385$ ,  $g_c = 1.5$  N/mm and  $l = 0.04$  mm. A small ‘ $k$ ’ value of  $1 \times 10^{-5}$  is used with viscosity parameter ‘ $\eta$ ’ set to zero.

The specimen is discretized with 5000 linear triangular finite elements. Quasi-static loading is first applied with a displacement increment of  $4 \times 10^{-3}$  mm over 150 loading steps. Subsequently the increment is reduced to  $2 \times 10^{-4}$  mm for the remaining steps.

Fig. 3b displays the evolved crack phase field for the maximum imposed displacement of  $\bar{u} = 0.801$  mm. With increasing load, the specimen experiences necking in the center region where the damage begins to localize. With a small further increase of applied load, damage in the center reaches one and the specimen fails. The observed fracture surface is in good agreement with the results of Tang et al. (2019,



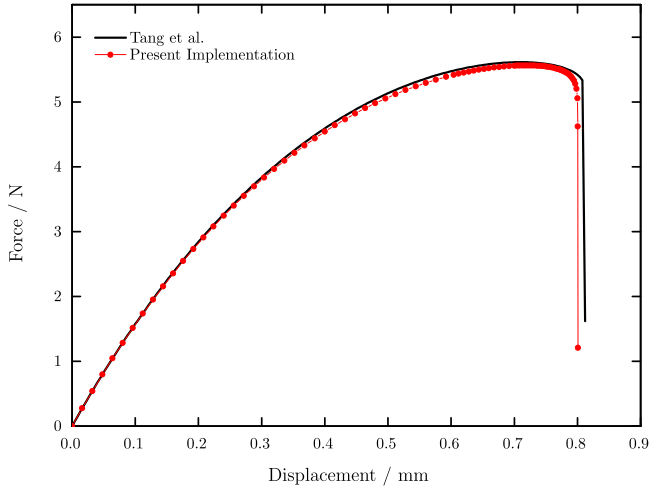


Fig. 4. Validation results of the tensile test shown in Fig. 3a. The force-displacement curves obtained with our numerical implementation match well with the original results of Tang et al. (2019). The force-displacement data of Tang et al. (2019) was obtained through private communication with the authors.

see Fig. 4 therein). The corresponding force-displacement curve of the simulated example is shown in Fig. 4. Again, the brutal nature of crack can be observed here and the results are in agreement with the ones of Tang et al. (2019), which validates the implemented methodology both qualitatively and quantitatively.

#### 4.2. Single-edge-notched shear test

In the previous example, only uniaxial tensile loading was involved, so that the entire energy contributes towards evolution of the crack phase field. In order to demonstrate the effects of tensile and compressive energy states, we now consider the single-edge-notched shear

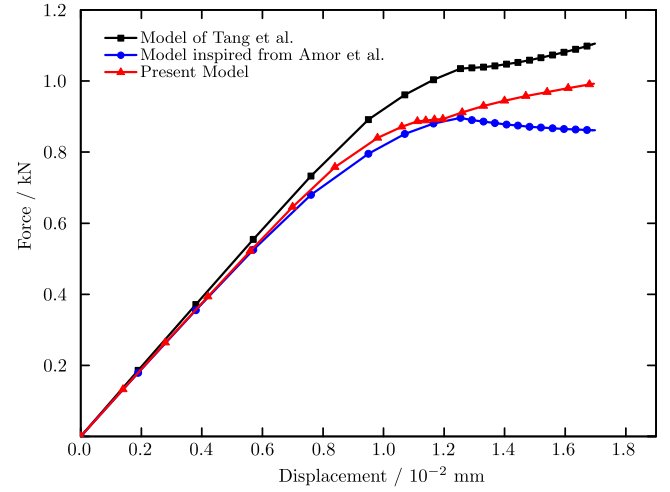


Fig. 6. Load-displacement curves obtained from the shear test by using the different splits discussed in Section 3. The post-critical behavior of the models discussed in Sections 3.1 and 3.3 is in accordance with the results of Miehe et al. (2010b).

test as done in Miehe et al. (2010b). The geometry and the boundary conditions of the test are shown in Fig. 2a.

As can be seen in the figure, the bottom edge of the specimen is fixed in both horizontal and vertical direction. A purely horizontal displacement load is applied on the top edge, which is additionally constrained in vertical direction. The specimen is discretized by approximately 20,000 linear triangular and quadrilateral finite elements with a finer mesh in the region where the crack is expected to propagate. The material parameters are given as  $\lambda = 121.15 \text{ kN/mm}^2$ ,  $\mu = 80.77 \text{ kN/mm}^2$ ,  $g_c = 2.7 \times 10^{-3} \text{ kN/mm}$  and  $l = 0.01 \text{ mm}$ . An incremental displacement loading as described in Miehe et al. (2010b) is applied to the specimen.

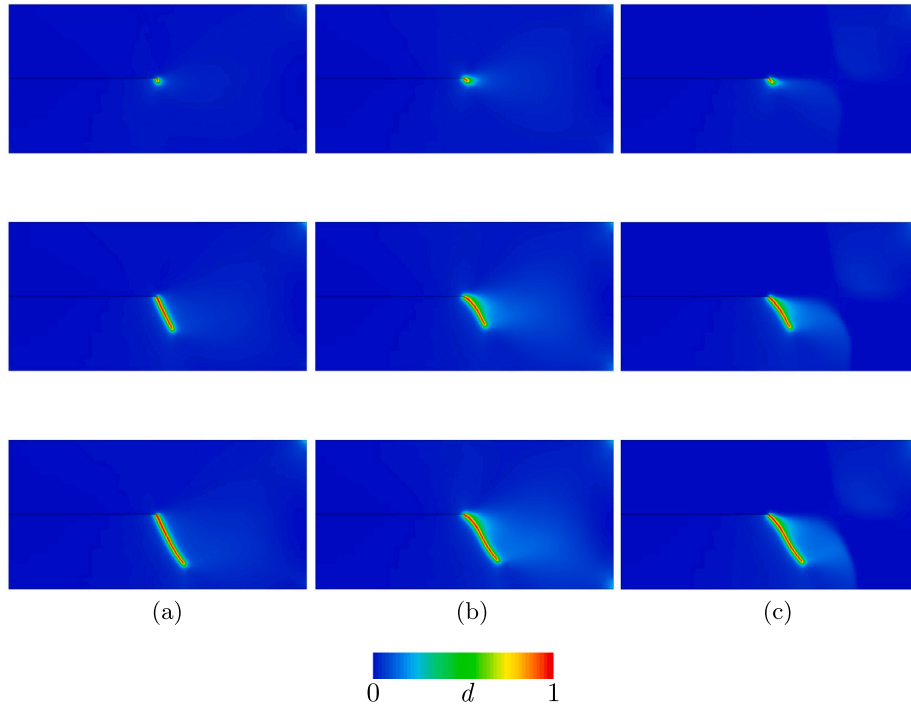


Fig. 5. Evolution of damage phase field in consideration of the different splits discussed in Section 3. The plotted crack patterns are related to applied displacements of  $\bar{u} = \{1.0, 1.4, 1.6\} \times 10^{-2} \text{ mm}$  (from top to bottom) in consideration of (a) the model of Tang et al. (2019), (b) the model inspired from Amor et al. (2009) and (c) the model proposed in Section 3.3.

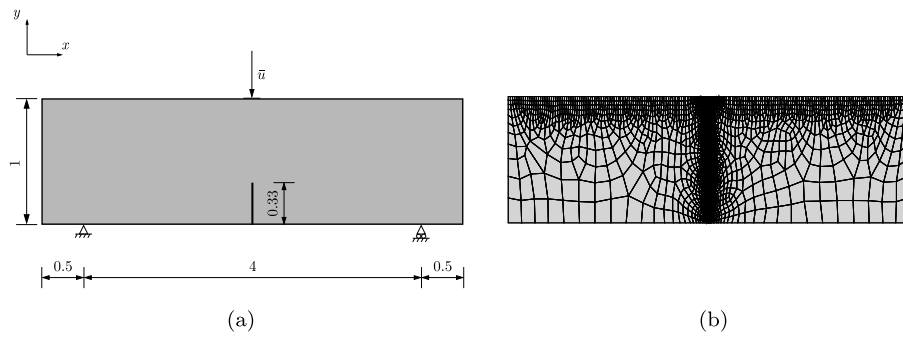


Fig. 7. Boundary-value problem of the three-point bending test. (a) Geometry and boundary conditions (units in mm) and (b) finite-element discretization of the domain with refined mesh in the area where the crack is expected to propagate.

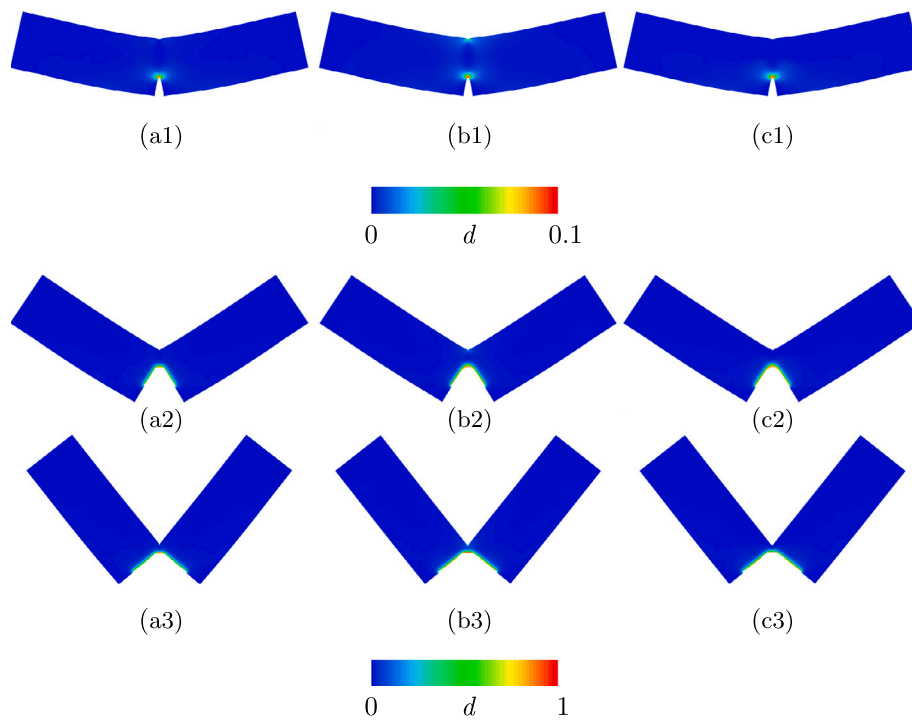


Fig. 8. Deformed specimens of the three-point-bending test shown in Fig. 7a. The plotted configurations are related to applied displacements of  $\bar{u} = \{0.4, 1.19, 1.9\}$  mm (from top to bottom) in consideration of (a) the model of Tang et al. (2019), (b) the model inspired from Amor et al. (2009) and (c) the model proposed in Section 3.3. The upper legend refers to the upper row of pictures, the lower legend refers to the middle and bottom row of pictures.

A ' $k$ ' value of  $1 \times 10^{-5}$  was used with the viscous regularization parameter ' $\eta$ ' set to  $2.5 \times 10^{-5}$  kNs/mm<sup>2</sup> as in Miehe et al. (2010b). The results of the problem under the implausible assumption of fracture driven by the total energy function was already shown in Fig. 2 where unphysical crack branching is observed.

A comparison of fracture evolution for the three models discussed in Sections 3.1–3.3 is depicted in Fig. 5 in consideration of three different levels of imposed displacements.

It is evident that all implemented splits permit physically plausible crack growth. Nevertheless, a slight variation is seen in the phase-field evolution of the model discussed in Section 3.2 in comparison with the other models. Observe that both the top right and the bottom right corner of the specimen exhibits damage when using the model of Section 3.2 (see Fig. 5b). This is in contrast to the results of the other two models (see bottom right corners of Fig. 5a and Fig. 5c), where compressive damage is entirely prohibited.

The associated load–displacement curves are shown in Fig. 6. It is discernible that the models allowing the use of only the tensile part of the energy towards creation of new crack surfaces clearly display a

stiffer response in the crack-propagation region. In contrast, the post-critical response of the model inspired from Amor et al. (2009) is rather compliant. This is because, for the same applied load, in addition to the propagating crack, damage also accumulates in the bottom right region as seen in Fig. 5b which manifests as reduced stiffness. Contrary to this, damage evolution in the other two models are local to the crack path resulting in higher reaction force response. This trend is also exhibited in the study performed in Miehe et al. (2010b), where the formulation that was restricted to only tensile-crack evolution showed a much stiffer response.

#### 4.3. Three-point bending test

To further demonstrate the capabilities of the new model, we investigate a classical three-point bending test subjected to large strains. The geometry and the boundary conditions of the simulation are as shown in Fig. 7a. The specimen is fixed along the vertical direction at the two bottom supports and the left support is additionally constrained in horizontal direction. Monotonically increasing displacement loading is

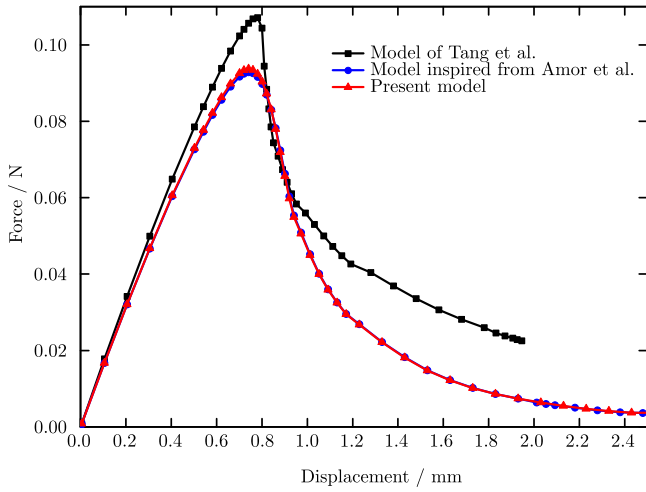


**Fig. 9.** Comparison of force-displacement curves of the three-point-bending test obtained for three different splits using the neo-Hookean strain-energy formulation. The model of Tang et al. (2019) was simulated by using the specific form of the energy-density function (17). This function is different to the energy function (29) used for the other two models, which explains the quantitatively different results.

applied at the center of the upper boundary of the specimen. A vertical slit is inserted at the lower boundary to create a pre-crack of appropriate length. The used finite-element mesh consists of approximately 7500 linear quadrilateral elements and the element size ( $h$ ) is refined in the region where crack is expected to propagate as indicated in Fig. 7b with  $l/h \approx 2$ .

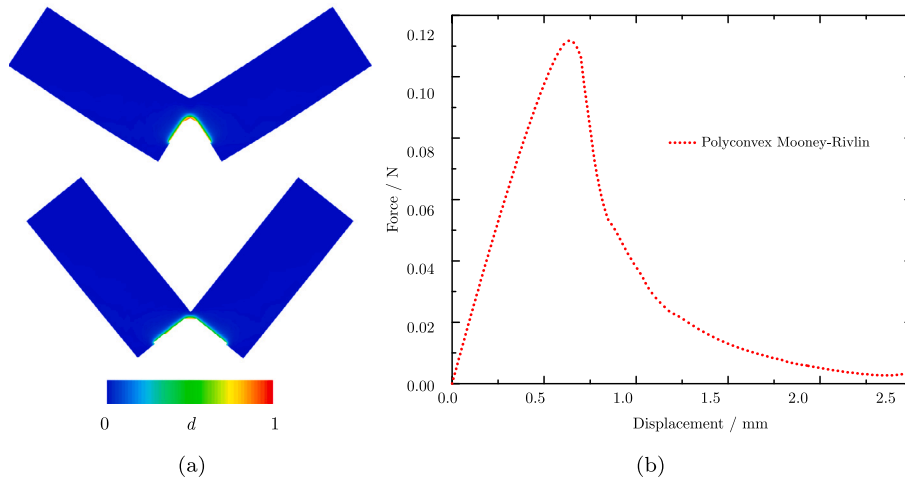


**Fig. 10.** Simulation results of the three-point bending test obtained with a polyconvex Mooney–Rivlin model. (a) Deformed configurations of the specimen in two different fractured states. The contour shows the magnitude of the evolved phase-field, where finite elements with  $d > 0.98$  are blanked to visualize the crack. (b) Force-displacement response showing the typical post-critical behavior.

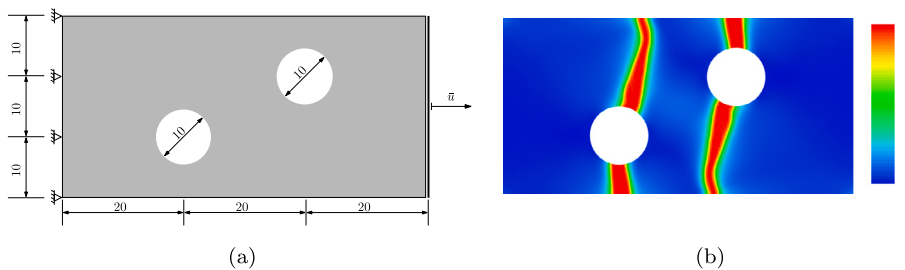


**Fig. 11.** Soft strip with two holes under tensile loading. (a) Dimensions of the specimen together with boundary conditions (units in mm) and (b) contour of the final damage phase field plotted onto the undeformed reference configuration.

Plane-strain conditions are assumed and the material parameters used in the simulation are  $\kappa = 4.03$  MPa,  $\mu = 1.86$  MPa,  $g_c = 7.5 \times 10^{-2}$  N/mm and  $l = 0.02$  mm. We have further employed a viscous regularization parameter of  $\eta = 1 \times 10^{-5}$  N s/mm<sup>2</sup> with ' $k$ ' =  $5 \times 10^{-4}$  to prevent complete loss of stiffness in a fully damaged element. Initially, an incremental displacement of  $\Delta u = 1 \times 10^{-4}$  mm is applied until crack initiation and subsequently reduced to  $1 \times 10^{-5}$  mm during the crack-propagation phase.

The evolution of the crack phase field for different displacement loading conditions is shown in Fig. 8. The crack path obtained using all three models is identical. Although not pronounced, a compressive damage is observed in the region where the specimen is loaded when using the model discussed in Section 3.2. On the other hand, when using the other models, this problem is alleviated (please refer to Fig. 8a1 and Fig. 8c1). We conclude that the newly proposed split can distinguish the local state of tension and compression in an accurate manner. For illustration purposes, regions of the continuum being damaged with  $d > 0.98$  are removed to visualize the crack propagation. Fig. 8a2 through Fig. 8c3 compare damage evolution among the three models for increasing values of applied displacements.

The force-displacement results obtained from the different models can be seen in Fig. 9. The differences between the results obtained using the model from Section 3.1 and the other models is attributed to the fact that the former was simulated using a specific form of neo-Hookean energy-density as given in Eq. (17), while the results of the other cases have been obtained by using the classical compressible neo-Hookean form as expressed in Eq. (29). Nevertheless, we observe that qualitatively all the models exhibit the same characteristics with physically meaningful behavior.



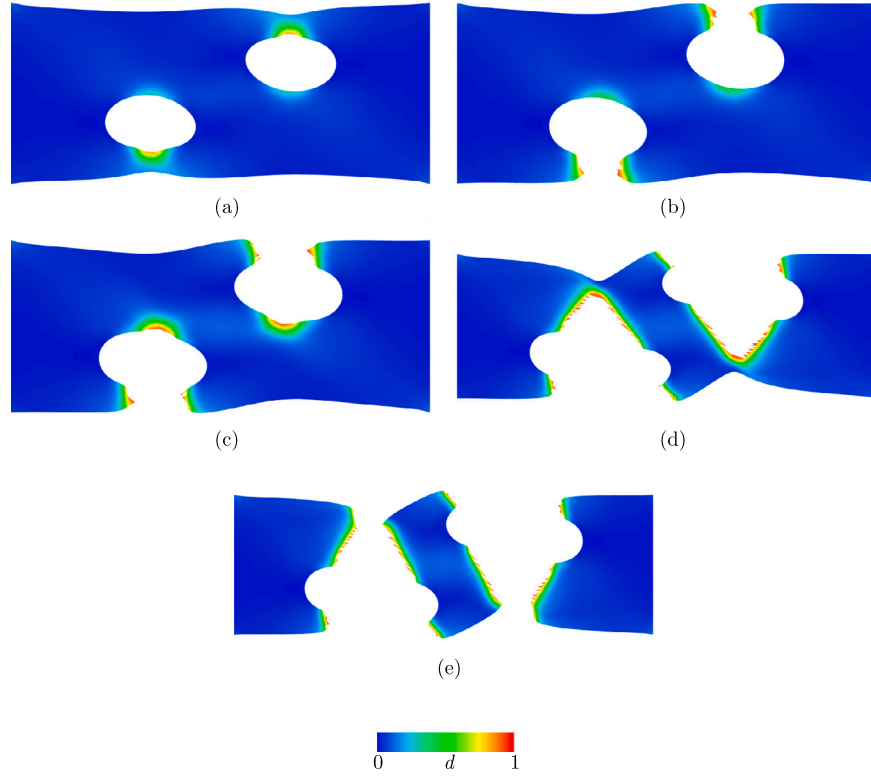


**Fig. 12.** Deformed configurations of the soft strip under tensile loading. From (a) to (e), the evolution of cracks until complete rupture of the strip is depicted, where finite elements with damage phase field  $d > 0.95$  are blanked to visualize the crack. The contour refers to the magnitude of the damage phase field.

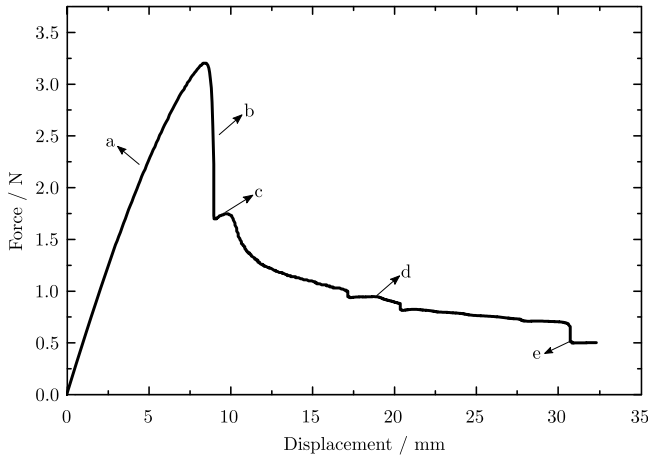


**Fig. 13.** Force-displacement curve related to the tension test on the soft inhomogeneous strip. The part indicated by “a” corresponds to the initial nonlinear elastic response. The force drop at position “b” indicates an instantaneous loss of stiffness due to the first crack set originating from the outer sides of the holes. The bump at “c” is due to recovery of elastic stiffness until the second set of cracks is initiated. The extensive region labeled with “d” corresponds to gradual stiffness reduction due to stable crack growth. Finally, at “e”, unstable crack propagation leading to complete rupture of the strip is observed. The regions “a” to “e” correspond to the images shown in Fig. 12. The remaining reaction force after complete failure is due to the chosen value of ‘ $k$ ’, which guarantees stable response in regions with  $d = 1$ .

#### 4.4. Demonstration with polyconvex Mooney–Rivlin model

The capability of the newly proposed model to distinguish tensile and compressive contributions using the classical neo-Hookean material has been demonstrated in the previous examples. In the present section, the transferability of the split to hyperelastic models containing

also the second invariant of the right Cauchy–Green deformation tensor  $\mathbf{C}$  is discussed. To this end, we consider a polyconvex two-parameter Mooney–Rivlin model according to<sup>7</sup> Hartmann and Neff (2003)

$$\psi_{\text{MR}}(I_1, I_2, J) = C_{10}(\bar{I}_1 - 3) + C_{01}(\bar{I}_2^{\frac{3}{2}} - 3^{\frac{3}{2}}) + \frac{\kappa}{2}(J - 1)^2, \quad (30)$$

where  $C_{10}$  and  $C_{01}$  are material parameters.

The above model in conjunction with the newly proposed split is now applied to the three-point bending test documented in the previous section. The material parameters were taken to be  $C_{10} = 0.6$  MPa and  $C_{01} = 0.33$  MPa such that the initial shear modulus  $\mu = 2(C_{10} + C_{01})$  is satisfied. Contour plots of the damage evolution are shown in Fig. 10a. As with the previous case, propagation of crack until the final moment of failure is illustrated where regions of the body with a damage field  $d > 0.98$  are removed to visualize the crack. We again observe that the boundary-value problem involves extremely large deformations which highlights the robustness of the proposed methodology. The corresponding force-displacement curve plotted in Fig. 10b shows a typical post-critical response.

#### 4.5. Inhomogeneous soft strip under tension

To further demonstrate the capability of the tension-compression split in conjunction with the Mooney–Rivlin model, we analyze a rectangular strip with two holes subjected to tensile loading as discussed in Miehe et al. (2015b). The dimensions of the specimen and the boundary conditions are as indicated in Fig. 11a.

<sup>7</sup> Please note that the simplest form of the two-parameter Mooney–Rivlin model

$$\psi_{\text{MR}}(I_1, I_2, J) = C_{10}(\bar{I}_1 - 3) + C_{01}(\bar{I}_2 - 3) + \frac{\kappa}{2}(J - 1)^2$$

is not polyconvex (Hartmann and Neff, 2003) and therefore not suitable for the present purposes.

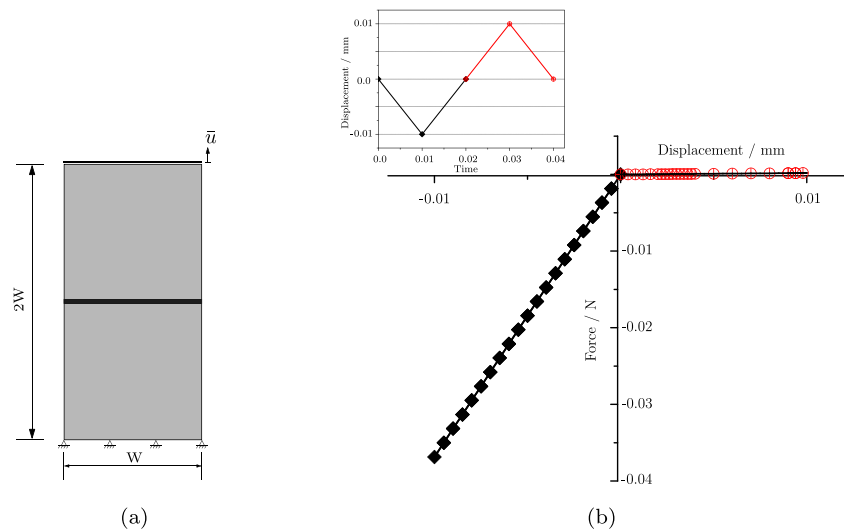


Fig. A.14. (a) Geometry and boundary conditions of the specimen with a through-crack in the center. (b) Loading and the associated force–displacement response.

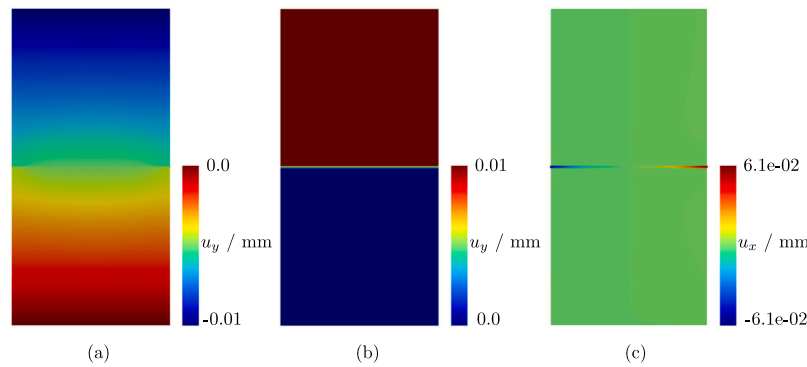


Fig. A.15. Contour plots of displacement (a) in the loading direction at the trough point indicating load transfer, (b) in the loading direction at the crest point indicating no load transfer and (c) in the lateral direction at the trough point indicating unconstrained expansion of broken elements.

The material parameters are selected to  $C_{01} = 0.065$  MPa,  $C_{10} = 0.03$  MPa (resulting in an initial shear modulus of  $\mu = 0.19$  MPa),  $g_c = 0.25$  N/mm and  $l/h = 2$ . A ' $k$ ' value of  $3 \times 10^{-3}$  was used in addition to the viscous regularization parameter ' $\eta$ ' of  $1 \times 10^{-3}$  N s/mm<sup>2</sup> as in [Tian et al. \(2020\)](#).

Due to the eccentricity of the holes an asymmetric stress state develops in the consequence of loading. The evolution of the crack phase field for increasing displacements is shown in [Fig. 12](#). It is to note that no pre-crack is introduced in the geometry of the strip.

As the applied displacement increases, cracks initiate from the outer boundaries of the holes ([Fig. 12a](#)) and start to grow towards the boundary of the strip ([Fig. 12b](#)). With the addition of further load, cracks now begin to develop on the inner boundaries of the eccentric holes as shown in [Fig. 12c](#). These cracks then start to grow towards the opposite edges of the strip which leads to a gradual loss of load-bearing capability. This corresponds to the region indicated as “d” in the plot of the reaction force shown in [Fig. 13](#). As the loading accumulates, complete rupture of the sample into three constituent pieces is seen, as depicted in [Fig. 12e](#). As before, to clearly visualize the crack path, elements with phase field  $d > 0.95$  are removed from the body. The evolved crack phase field under fully applied loading is shown with respect to the geometry of the reference configuration in [Fig. 11b](#). The results obtained in the present work fit very well to what was reported in [Miehe et al. \(2015b\)](#).

For completeness, the reaction force as a function of applied displacement is plotted in [Fig. 13](#), where distinct regions of crack propagation can be clearly distinguished.

## 5. Conclusion

We presented a novel way of decomposing an energy density into tensile and compressive parts in the context of the phase-field approach to fracture at finite deformations. The salient features of the proposed model are that the sum of the tensile and the compressive parts strictly add up to the undamaged total reference energy and that it can be applied to a large variety of finite-strain energy densities. Qualitative and quantitative comparisons of the proposed model with existing models were performed and the differences with respect to existing variants were highlighted. Several representative examples were simulated that substantiate the capability of the proposed model to accurately account for distinct energy terms in an adequate manner. The predicted fracture patterns and force–displacement results agree well with those found in literature. Future work will point towards the extension of the given formulation to model fatigue and plasticity.

## Declaration of competing interest

The authors declare that they have no known competing financial interests or personal relationships that could have appeared to influence the work reported in this paper.

## Acknowledgments

Shreeraman Swamynathan and Sebastian Jobst acknowledge the financial support provided for this work by the Automotive Electronics

division of 'Robert Bosch GmbH', Germany. Shreeraman Swamynathan acknowledges several meaningful discussions and assistance received from M.Sc. Daniel Kienle and Dipl.-Ing. Stephan Teichtmeister from the 'Chair of Materials Theory' of the 'University of Stuttgart'.

## Appendix. Distinction of tension and compression behavior

Here, we demonstrate the ability of the proposed approach in Section 3.3 to distinguish tensile and compressive loading.

To this end, we consider a 2D plate with a through-crack modeled in the center using Dirichlet boundary condition as in Fig. A.14a. The simulation was carried out with polyconvex Mooney–Rivlin model with parameters as in Section 4.4. The top edge is subjected to time varying displacement loading as shown in Fig. A.14b. Under compression, we can observe that the load is transmitted resulting in a stiff reaction force response. In contrast, under tension negligibly small load is transferred due to the small value of  $k = 5 \times 10^{-5}$  that guarantees small rest-elastic stiffness in the fully broken state. The performance of the split can also be seen in the displacement contour plots in the loading direction as shown in Fig. A.15a, b. They correspond to the trough and crest point of the loading cycle respectively. In Fig. A.15c, the lateral displacements corresponding to the trough point are depicted where unphysical lateral expansion is observed as documented in Steinke and Kaliske (2019). Nevertheless, we believe such numerical artefacts in the fully degraded elements have negligible effect on the quantitative response of the model.

## References

- Ambati, M., Kruse, R., De Lorenzis, L., 2016. A phase-field model for ductile fracture at finite strains and its experimental verification. *Comput. Mech.* 57 (1), 149–167.
- Amor, H., Marigo, J.-J., Maurini, C., 2009. Regularized formulation of the variational brittle fracture with unilateral contact: Numerical experiments. *J. Mech. Phys. Solids* 57 (8), 1209–1229.
- Ball, J.M., 1976. Convexity conditions and existence theorems in nonlinear elasticity. *Arch. Ration. Mech. Anal.* 63 (4), 337–403.
- Bilgen, C., Weinberg, K., 2019. On the crack-driving force of phase-field models in linearized and finite elasticity. *Comput. Methods Appl. Mech. Engrg.* 353, 348–372.
- Bleyer, J., Alessi, R., 2018. Phase-field modeling of anisotropic brittle fracture including several damage mechanisms. *Comput. Methods Appl. Mech. Engrg.* 336, 213–236.
- Bourdin, B., Francfort, G.A., Marigo, J.-J., 2000. Numerical experiments in revisited brittle fracture. *J. Mech. Phys. Solids* 48 (4), 797–826.
- Bourdin, B., Larsen, C.J., Richardson, C.L., 2011. A time-discrete model for dynamic fracture based on crack regularization. *Int. J. Fract.* 168 (2), 133–143.
- Francfort, G.A., Marigo, J.-J., 1998. Revisiting brittle fracture as an energy minimization problem. *J. Mech. Phys. Solids* 46 (8), 1319–1342.
- Griffith, A.A., 1921. VI. The phenomena of rupture and flow in solids. *Philos. Trans. R. Soc. Lond. A* 221 (582–593), 163–198.
- Gültekin, O., Dal, H., Holzapfel, G.A., 2016. A phase-field approach to model fracture of arterial walls: theory and finite element analysis. *Comput. Methods Appl. Mech. Engrg.* 312, 542–566.
- Gürses, E., Miehe, C., 2009. A computational framework of three-dimensional configurational-force-driven brittle crack propagation. *Comput. Methods Appl. Mech. Engrg.* 198 (15–16), 1413–1428.
- Hartmann, S., Neff, P., 2003. Polyconvexity of generalized polynomial-type hyperelastic strain energy functions for near-incompressibility. *Int. J. Solids Struct.* 40 (11), 2767–2791.
- Hesch, C., Gil, A., Ortigosa, R., Dittmann, M., Bilgen, C., Betsch, P., Franke, M., Janz, A., Weinberg, K., 2017. A framework for polyconvex large strain phase-field methods to fracture. *Comput. Methods Appl. Mech. Engrg.* 317, 649–683.
- Hesch, C., Weinberg, K., 2014. Thermodynamically consistent algorithms for a finite-deformation phase-field approach to fracture. *Internat. J. Numer. Methods Engrg.* 99 (12), 906–924.
- Hofacker, M., Miehe, C., 2012. Continuum phase field modeling of dynamic fracture: variational principles and staggered FE implementation. *Int. J. Fract.* 178 (1–2), 113–129.
- Kuhn, C., Noll, T., Müller, R., 2016. On phase field modeling of ductile fracture. *GAMM-Mitt.* 39 (1), 35–54.
- Kuhn, C., Schlüter, A., Müller, R., 2015. On degradation functions in phase field fracture models. *Comput. Mater. Sci.* 108, 374–384.
- Miehe, C., Hofacker, M., Schänzel, L.-M., Aldakheel, F., 2015a. Phase field modeling of fracture in multi-physics problems. Part ii. coupled brittle-to-ductile failure criteria and crack propagation in thermo-elastic-plastic solids. *Comput. Methods Appl. Mech. Engrg.* 294, 486–522.
- Miehe, C., Hofacker, M., Schänzel, L.-M., Aldakheel, F., 2015b. Phase field modeling of fracture in multi-physics problems. Part ii. coupled brittle-to-ductile failure criteria and crack propagation in thermo-elastic-plastic solids. *Comput. Methods Appl. Mech. Engrg.* 294, 486–522.
- Miehe, C., Hofacker, M., Welschinger, F., 2010a. A phase field model for rate-independent crack propagation: Robust algorithmic implementation based on operator splits. *Comput. Methods Appl. Mech. Engrg.* 199 (45–48), 2765–2778.
- Miehe, C., Schänzel, L.-M., 2014. Phase field modeling of fracture in rubbery polymers. Part i: Finite elasticity coupled with brittle failure. *J. Mech. Phys. Solids* 65, 93–113.
- Miehe, C., Welschinger, F., Hofacker, M., 2010b. Thermodynamically consistent phase-field models of fracture: Variational principles and multi-field FE implementations. *Internat. J. Numer. Methods Engrg.* 83 (10), 1273–1311.
- Raina, A., Miehe, C., 2016. A phase-field model for fracture in biological tissues. *Biomech. Model. Mechanobiol.* 15 (3), 479–496.
- Steinke, C., Kaliske, M., 2019. A phase-field crack model based on directional stress decomposition. *Comput. Mech.* 63 (5), 1019–1046.
- Storm, J., Supriatna, D., Kaliske, M., 2020. The concept of representative crack elements for phase-field fracture: Anisotropic elasticity and thermo-elasticity. *Internat. J. Numer. Methods Engrg.* 121 (5), 779–805.
- Strobl, M., Seelig, T., 2015. A novel treatment of crack boundary conditions in phase field models of fracture. *Pamm* 15 (1), 155–156.
- Strobl, M., Seelig, T., 2016. On constitutive assumptions in phase field approaches to brittle fracture. *Procedia Struct. Integr.* 2, 3705–3712. <http://dx.doi.org/10.1016/j.prostr.2016.06.460>, URL: <http://www.sciencedirect.com/science/article/pii/S2452321616304796>, 21st European Conference on Fracture, ECF21, 20–24 June 2016, Catania, Italy.
- Tang, S., Zhang, G., Guo, T.F., Guo, X., Liu, W.K., 2019. Phase field modeling of fracture in nonlinearly elastic solids via energy decomposition. *Comput. Methods Appl. Mech. Engrg.* 347, 477–494.
- Taylor, R.L., 2017. FEAP – Finite Element Analysis Program. University of California, Berkeley, URL: <http://www.ce.berkeley/feap>.
- Teichtmeister, S., Kienle, D., Aldakheel, F., Keip, M.-A., 2017. Phase field modeling of fracture in anisotropic brittle solids. *Int. J. Non-Linear Mech.* 97, 1–21.
- Tian, F., Tang, X., Xu, T., Li, L., 2020. An adaptive edge-based smoothed finite element method (ES-FEM) for phase-field modeling of fractures at large deformations. *Comput. Methods Appl. Mech. Engrg.* 372, 113376.
- Yin, B., Kaliske, M., 2020. Fracture simulation of viscoelastic polymers by the phase-field method. *Comput. Mech.* 65 (2), 293–309.